Evidence for controlled insertion of Fe ions in the framework of clinoptilolite natural zeolites

Graphical abstract

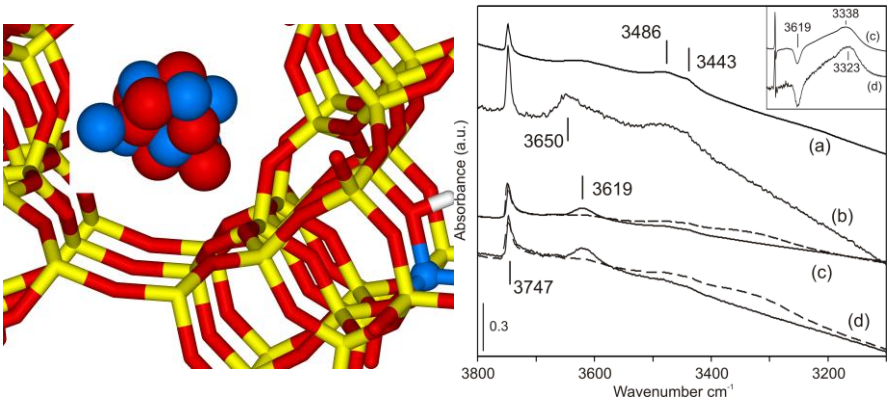

A combined structural and spectroscopic study on Fe-containing natural zeolites allowed to describe a complex distribution of iron oxide clusters and nanoparticles and to prove the insertion of Fe^{3+} ions in tetrahedral framework positions.

Evidence for controlled insertion of Fe ions in the framework of clinoptilolite natural zeolites.

F. Chávez-Rivas,[1,§] G. Rodríguez-Fuentes,[2] G. Berlier,[1*] I. Rodríguez-Iznaga,[2] V. Petranovskii,[3] R. Zamorano-Ulloa,[4] and S. Coluccia[1]

[1] Dipartimento di Chimica and NIS Centre of Excellence , Università di Torino, Via P. Giuria 7, 10125 Torino, Italy;

[2] Instituto de Ciencia y Tecnología de Materiales (IMRE), Universidad de La Habana, Zapata y G, s/n. Ciudad de La Habana 10400, Cuba

[3] Universidad Nacional Autónoma de México, Centro de Nanociencias y Nanotecnología, Apdo. Postal 14, C.P. 22800, Ensenada, B.C., México

[4] Departamento de Física, Escuela Superior de Física y Matemáticas del IPN, 07738, México D.F., México

[§] On sabbatical leave, granted by ESFM-IPN, México, D. F

[*] corresponding author, e-mail: gloria.berlier@unito.it, tel.: 0039 0116707856, fax.: 0039 0116707953

Abstract

This work is focused on the spectroscopic characterization of a set of materials obtained by hydrothermal treatments from a natural clinoptilolite zeolite, NZ. OPAZ (orthophosphoric acid treatment on NZ), Fe^{2+}-OPAZ (ferrous sulphate acid treatment on OPAZ) and Fe^{3+}-OPAZ (ferric sulphate acid treatment on OPAZ) samples were characterized by HRTEM, UV-Vis, temperature dependent EPR and Infra Red spectroscopies in order to describe the structure, nuclearity and distribution of iron ions and iron oxides clusters and particles. Complementary pieces of information were obtained from the different techniques. In particular, HRTEM analysis suggested an effect of the hydrothermal treatments not only on the Fe speciation but also on the zeolite particles morphology and surface. The same technique could not clearly detect the presence of iron oxide phases, suggesting their very small size and high dispersion. A more detailed description of the isolated and clustered species could be in turn obtained by UV-Vis spectroscopy. This was confirmed by temperature dependent EPR spectroscopy, suggesting the presence of nanosized ferromagnetic magnetite-like particles. Finally, IR spectroscopy gave clear cut evidence about the insertion of Fe^{3+} ions in framework positions, with consequent generation of distinct Brønsted acidity, after hydrothermal treatments with iron salts. This transformation could be explained through the reaction with defective hydroxyl nests formed by mildly acid hydrothermal treatment with isolated Fe^{3+} ions.

Keywords: natural zeolites, iron, FTIR, EPR, HRTEM

1. Introduction

Among sedimentary zeolite tuffs, the more important structures, as regarding their occurrence and practical applications, are clinoptilolite, chabazite, mordenite and phillipsite [1]. The main applications are in the environmental field, particularly for soil amendment, cement manufacture and wastewater purification. The diversity of natural and artificial zeolites [2,3], presents inexhaustible research field of nanomaterials synthesis with controlled chemical, catalytic, optical, and magnetic properties [4-6]. Transition metal ions and nanoparticles within nanoporous media like zeolites are efficient modifiers of their properties. Heulandite and the isostructural clinoptilolite (IUPAC code HEU [3]) are widely used natural zeolite tuff, thanks to their selective cation-exchange properties and to their widespread availability.

As for chemical composition, it is well known that natural zeolite tuffs contain iron, as recently discussed by Prof. Vezzalini [7]. However, the exact location of iron in natural zeolites, and the ability to control its distribution, have not been completely clarified up to the date. This knowledge could be crucial to influence physical-chemical properties and to design materials for precise applications, such as catalysis and photocatalysis [8,9].

It is worth to mention that the incorporation of iron into the framework of synthetic zeolites has been a hot topic in recent years, due to the catalytic activity of Fe-zeolites in selective oxidation reactions and NO_x Selective Catalytic Reduction [10,11]. The debate about the nature of the catalytically active sites, isolated Fe^{2+} ions or dimeric-oligomeric species in extra-framework positions, has resulted in a incredibly high number of publications on the subject [12,13], as recently reviewed [14]. This interest has also leaded to the development of new ways to introduce Fe species in zeolitic frameworks in controlled manner [15,16]. This huge effort in understanding the structure and chemical reactivity of highly dispersed Fe sites has not been applied to natural zeolites up to now.

Many studies have been carried out to elucidate the influence of iron species on the thermal stability of natural Cuban clinoptilolite, contained in the zeolite tuff from the Tasajeras deposit of

Villa Clara province, Cuba. However, the high content of iron species (mainly in the form of iron oxide and oxyhydroxides complex), prevented the determination of isolated iron species in framework and extra framework positions. Thus, in a recent work we proposed a new strategy based on a hydrothermal mild acid treatment, to remove most of the iron [17]. Subsequently, iron was inserted in a controlled manner, by a similar hydrothermal acid treatment with ferrous and ferric sulphate. Different characterization techniques suggested the location of Fe^{3+} iron ions in the framework of clinoptilolite structure, and demonstrated the feasibility of removing and reinserting Fe ions in a controlled manner [17].

The aim of this work is thus to improve our knowledge about the structure and distribution of Fe species in natural zeolite (NZ) clinoptilolite samples, with particular attention to the effect of hydrothermal treatments on controlled iron re-insertion. More in detail, different spectroscopies (Diffuse Reflectance UV-Vis, temperature dependent EPR and IR), coupled to High Resolution Transmission Microscopy (HRTEM) were employed to give a precise description of both isolated and clustered moieties in very complex systems.

2. Experimental section

NZ material is a purified zeolite material - clinoptilolite type - obtained from the zeolitic rock from Tasajeras deposit (Cuba). The purification of the crystalline clinoptilolite phase is described in Ref. [18], with the important additional step of the extraction of iron oxide particles using a strong magnet. Thus, purified NZ sample contains 78 % clinoptilolite-heulandite (HEU under IUPAC code), 4% mordenite and 17% for quartz plus feldspar plus montmorillonite and iron oxide.

Hydrothermal treatments were carried out as described in Ref [17], and detailed in the following. NZ sample (Si/Al = 5.8, Fe = 1.65 wt%) was modified in a glass reactor using diluted orthophosphoric acid (87 wt %). The final concentration of phosphoric acid was fixed at six phosphorus atoms per clinoptilolite unit cell, and the solid/solution ratio was 0.1. The hydrothermal

reaction took place between 70° and 100°C at open air. After the reaction the samples were washed until no acid residues were detected in water. The final pH of sample slurry (10 wt % of solid in water) was fixed at 5.6. The solid was filtered and dried at 160°C up to a 2% residual humidity. The time and temperature of the reaction were established considering the efficiency of the iron extraction process in the zeolite. The best sample with the lowest iron content was labeled as OPAZ (Si/Al = 3.6, Fe < 0.005 wt%). OPAZ sample was modified in the same hydrothermal conditions with 0.5 M $FeSO_4$ or $Fe_2(SO_4)_3$ solutions, buffered with H_2SO_4 at pH 1.2. The resulting samples are hereafter labeled as Fe^{2+}-OPAZ (Si/Al = 3.14, Fe = 0.41 wt%) and Fe^{3+}-OPAZ (Si/Al = 3.59, Fe = 5.03 wt%), respectively. All samples were dried at 160ºC.

Diffuse reflectance UV-Visible (DR UV-Vis) spectra were collected on a Varian Cary 300 equipped with a standard DR unit using a barium sulphate reference in the wavelength range 190-850 nm. The spectra were measured on hydrated powder samples under ambient conditions and were deconvoluted to Gaussian functions using the Peak Fitting module of Origin Pro 8 Software (version 8, Microcal Software, Inc., Northampton, MA, USA).

EPR spectra of air-exposed hydrated and dehydrated samples (in a muffle at 393 K for 5 h), were measured between 300 and 77 K with a JEOL JES-RE3X spectrometer at a frequency of 9 GHz, power of 1 mW and modulation frequency of 100 KHz. Low temperature EPR spectra were settled by flowing vapour of liquid N_2 with a stable temperature of ± 1 K. The g values were determined in comparison with a small signal of the standard DPPH (g = 2.0036). Reported EPR spectra were normalized to the mass. The analysis of the ferromagnetic component found between 220 and 100 K (shown in inset of Fig. 4), was obtained by subtracting the signal at g_{eff} = 4.3 obtained from its corresponding EPR signal at 77 K and multiplied by convenient modulated factors. The same method was employed for the subtraction of the signal at g_{eff} = 2 but using its corresponding EPR signal at room temperature, by employing the Esprit-425 Jeol software [19].

High Resolution Transition Electron Microscope (HRTEM) images were registered with a JEOL 3010-UHR with acceleration potential of 100 kV, by dispersing the powdered samples on a

copper grid covered with a lacey carbon film. Measurements were also performed at 300 kV, but under these conditions the collapse of the zeolite framework under electronic irradiation was observed.

Fourier Transform Infra Red (FTIR) experiments were carried out on a Bruker IFS 28 spectrophotometer equipped with a cryogenic MCT detector, working with resolution of 2 cm^{-1} over 64 scans. The samples were in the form of thin self-supporting pellets (5-10 mg/cm^2) suitable for transmission IR experiments. Samples were directly treated in a quartz cell equipped with KBr windows, designed for room temperature (RT) and liquid nitrogen temperature (LNT) studies in controlled atmosphere. The samples were treated under dynamic vacuum up to 550 °C, where oxidation took place (60 Torr of O_2 for 1 hour). The reported IR spectra were normalized with respect to the intensity of the overtone framework modes at 1872 cm^{-1} [20].

3. Results

3.1. DR UV-Vis spectroscopy

The UV-Vis spectra of NZ and its modified hydrothermal forms OPAZ, Fe^{2+}-OPAZ and Fe^{3+}-OPAZ are shown in Fig. 1. The spectra present complicated absorption bands, as often observed in iron containing zeolites, implying the presence of heterogeneous systems. There is a general agreement in the literature about the fact that the bands position could be employed to estimate the nuclearity of supported Fe_xO_y moieties [12,14,21-24], as will be detailed in the following.

Spectral deconvolution was carried out on the whole set of data, by employing the lowest number of Gaussian sub-bands, as exemplified in Fig. 2 for Fe^{2+}-OPAZ sample. The corresponding spectrum is characterized by a main absorption with maxima at 215 and 270 nm, a shoulder at 350 nm, an important tail up to 500 nm and an almost constant plateau up to 850 nm. The fitting below 300 nm was done using three Gaussian bands with maxima at 211, 252 and 285 nm, while three broad sub-bands with maxima at 338, 427 and 700 nm were necessary to fit the tail up to 800 nm.

Similar results were obtained by fitting the experimental spectra of NZ and OPAZ samples: while the high energy components showed almost coincident frequency in the three samples, small modifications were found for the three low energy components (343, 459 and 700 nm for OPAZ, 343, 439 and 726 nm for NZ).

According to the literature, the bands at 211 and 252 nm belongs to oxygen-to-iron CT of isolated Fe^{3+} ions in tetrahedral coordination, while the band at 285 nm can be associated to CT of octahedral Fe^{3+} ions/nanoclusters [21-24], or to dimeric clusters [25]. These bands can be thus taken as a fingerprint of highly dispersed Fe ions, both in framework (211 and 252 nm) and extra framework positions (285 nm), even if the high energy component (211 nm) has to be considered with great care with respect to maximum position, due to the low instrumental sensitivity in this high energy region.

The band around 340 nm can be assigned to octahedral Fe ions in oligomeric clusters of Fe_xO_y-type inside the channels [24,25], while the bands at higher wavenumbers testify or a more extensive clustering of oligomeric iron clusters, finally giving Fe_2O_3 particles located on the external surface of the zeolite crystals [25,26]. As for the broad absorption between 600 and 800 nm, being very weak on Fe^{2+}-OPAZ sample, it closely reminds of the spectra reported by Sherman and Waite on Fe^{3+} oxides and hydroxides, which were assigned to ligand field *d-d* transitions, strongly intensified by magnetic coupling of adjacent Fe^{3+} cations [27,28].

These pieces of information can be employed to compare the Fe distribution in the different samples. NZ sample shows, together with the CT bands of tetrahedral Fe^{3+} ions, a large fraction of bigger oxide agglomerates, with high heterogeneity in sizes and chemical complexity. Particularly, we acknowledge the broad and intense contributions at 350-550 nm and 600-880 nm. The latter, in particular, testifies of relatively large iron oxide particles. After the hydrothermal treatment necessary to remove most of iron (passing from 1.65 to < 0.05 wt%), OPAZ sample mainly shows isolated Fe^{3+} ions, with small fractions of highly dispersed oligomeric clusters of different sizes. The concentration of isolated Fe^{3+} ions is increased after controlled reinsertion of iron in Fe^{2+}-

OPAZ sample. In this sample the concentration of oligomeric clusters is also consistent (tail up to 400 nm), while bigger agglomerates represent a minority. The high dispersion of species in this sample is in agreement with the low iron content (0.41 wt%).

More complicated is the situation of sample Fe^{3+}-OPAZ. In this case additional components are observed at 370, 438, 615 and 850 nm. In this case spectral deconvolution required a larger number of sub-bands and was not considered to be fully reliable. This sample is characterized by a very high iron amount (5.03 wt%) and by the presence of iron sulphate $Fe_2(SO_4)_3(OH)_5 \cdot 2H_2O$ crystalline particles [17], which could be the responsible for the additional bands at 370 and 438 nm. The presence of bands in the high (211 and 270 nm) and low (600-800 nm) frequency regions suggests the presence of both isolated Fe^{3+} ions and of iron oxide agglomerates, respectively.

These data confirm the effect of hydrothermal treatments in controlled removal and reinsertion of Fe species. It is noteworthy that the two iron salts give quite different iron distributions, which are however characterized by the same oxidation state (3+). This can be explained by the chemistry of iron ions in solution. While ferric ions tend to agglomerate (resulting in larger aggregation and high loading), we can propose that the gradual oxidation of Fe^{2+} to Fe^{3+} in solution allows a more controlled insertion.

3.2. EPR spectroscopy

The temperature dependent EPR spectra of NZ are shown in Fig. 3. All measurements consist of an intense broad asymmetric line, which shows, at 300 K, an effective splitting *g* value, g_{eff}, (defined by the zero crossing of the line base absorption) of 2.56 and a linewidth ΔH (defined between the maxima and minima of the absorption) of 166 mT. As the temperature decreases, the corresponding g_{eff} value and linewidth increase, reaching maximum values 77 K, with an overall reduction of the intensity. A similar trend with temperature was ascribed to dispersed and randomly oriented iron oxides magnetite-maghemite (Fe_3O_4, γ-Fe_2O_3) nanoparticles [29,30].

The same temperature dependent experiments were carried on the whole set of sample, as exemplified in Fig. 4, where the results obtained on Fe^{2+}-OPAZ sample are reported. Two signals at g_{eff} = 4.3 and g_{eff} = 2.0, assigned to a strongly distorted rhombic site (as in framework positions) and to bulk octahedral Fe^{3+} species (extraframework species), respectively are present. A thermally activated signal around g_{eff} = 13 is formed, reaching a maximum in intensity at 180 K and disappearing around 110 K. Similar results were obtained for OPAZ and Fe^{3+}-OPAZ samples.

The changes with temperature of this ferromagnetic resonance signal can be better appreciated in Fig. 4 inset, where the signals at g_{eff} = 4.3 and g_{eff} = 2.0 were removed (see experimental). In particular, the signal linewidth decreases with temperature, as a consequence of spin-lattice relaxation processes [31]. The signal reaches higher intensity around 180-170 K, with an asymmetric shape typical of ferromagnetic species (linewidth AH = 79 mT, g_{eff} = 12.7), shifting to lower fields at lower temperature (AH = 69 mT, g_{eff} = 15.7 at 130 K). The shape and trend with temperature of this feature very closely resemble that reported for bulk-like or nanosized magnetite [32-34]. Due to the broad character of the signal, a detailed assignment is quite delicate, since the EPR signal shape and intensity arise from many parameters, including the size of the ferromagnetic moieties and their distribution [35,36].

A further analysis of the broad signal around g_{eff} = 13 is carried out by comparing its maximum intensity (at 180 K) in the four samples object of this study (Fig. 5), showing the intensity order Fe^{2+}-OPAZ > OPAZ > Fe^{3+}-OPAZ. Since this feature is not observed on sample NZ, characterized by very broad signals and by the presence of big iron oxide aggregates (see UV-Vis), we can infer that the signal at g_{eff} = 13 is related to small ferromagnetic iron oxide nanoparticles, highly dispersed in the zeolites channels or on their external surface.

As for sample Fe^{3+}-OPAZ, it also depicts at g_{eff} = 2.0 a low intensity EPR signal with hyperfine structure having splitting characteristic of octahedral Mn^{2+} ions [37,38]. This assignment was confirmed by performing EPR measurements at 77 K on the hydrated and dehydrated sample

(see supplementary information), and suggests the insertion of Mn^{2+} impurities, which are probably stabilized by the zeolite framework as counterions.

3.3. HRTEM analysis

HRTEM analysis was carried out to get further information on the effect of the hydrothermal treatment on the zeolite morphology and on the size of Fe_xO_y particles. Some representative images have been selected for NZ, OPAZ and Fe^{2+}-OPAZ samples and are reported in Fig. 6.

NZ sample is formed by sub-micrometric aggregates, formed by zeolitic particles heterogeneous in size and shape (see Fig. S2). An example is reported in Figure 6a, showing part of a large regular crystalline particle (300 x 130 nm in size) with smaller irregular particles on its surface. In OPAZ sample, large aggregates of zeolitic particles are still present, but they look more disordered and in some parts covered by amorphous-like matter (Figs. S3 and S4), in agreement with the low stability of this sample [17]. However, well defined crystalline particles can be detected, as shown in Figure 6b.

Similarly, Fe^{2+}-OPAZ sample can be described as sub-micrometric aggregates, formed by large elongated particles (Fig. 6c and S5) and well defined hexagonal particles (Fig 6d) with size between 20 and 40 nm. On the whole, this sample shows a negligible amount of amorphous matter with respect to OPAZ sample, suggesting a dissolution effect of the treatment.

For all samples, the analysis of the diffraction distances by Fourier Transform (FT) analysis only resulted in distances typical of the clinoptilolite (HEU structure), particularly the (020), (200), (-312) and (-402) planes (measured distances at 8.95, 7.79, 3.60 and 3.36 nm, respectively) [39]. No evidence for any iron oxides phase could be obtained either by FT, suggesting very small particle size and high dispersion. This indicates that UV-Vis and EPR spectroscopies, showing a wide diversity of Fe_xO_y oligomeric clusters and nanoparticles are more sensitive, testifying of species which are below the detection limits of HRTEM.

3.4. Infra Red Spectroscopy

IR spectra in the OH stretching (νOH) region of the four zeolite samples are shown in Fig. 7. Before the measurements (and CO dosage) the samples were thermally activated and oxidized in vacuum to remove adsorbed water and impurities. The narrow peak at 3747 cm^{-1}, observed in all samples, is related to isolated Si–OH groups mainly present on the external surface of the zeolite particles [40,41]. The intensity of this band increases from NZ to OPAZ sample, suggesting an effect of the hydrothermal treatment on particle morphology, in agreement with TEM. This effect is less evident for Fe^{2+}-OPAZ and Fe^{3+}-OPAZ samples.

At lower energy, NZ is characterized by broad and weak features at 3468 and 3443 cm^{-1}, related to OH groups interacting by hydrogen bonding in hydroxyl nests [40,41]. These bands are more intense in sample OPAZ, testifying of an increase in the framework defectivity as a result of the acid treatment. In this line, the new band at 3650 cm^{-1} on OPAZ can be assigned to OH groups on defective Al^{3+} framework sites [42,43].

More interesting is the appearance, in Fe^{2+}- and Fe^{3+}-OPAZ samples, of a well-defined band at 3619 cm^{-1}, which can be assigned to bridging hydroxyl groups Si(OH)Fe, related to framework iron sites [21,44,45]. Upon CO dosage at 110 K (dashed lines and difference curves in Fig. 7 inset), the band at 3619 cm^{-1} disappears and a broad absorption centred at 3323/3338 cm^{-1} grows, as a result of the formation of hydrogen bonded OH··CO adducts. The measured shifts (297 cm^{-1} for Fe^{2+}-OPAZ and 281 cm^{-1} for Fe^{3+}-OPAZ) testify of the Brønsted acidity of the involved OH groups, in agreement with those observed for bridging hydroxyl groups Si(OH)T (T= Al, Fe, Ga etc) in synthetic zeolites or aluminophosphates [43-47]. This evidence demonstrates the reinsertion of Fe^{3+} ions in zeolite framework positions as a consequence of the hydrothermal treatments, irrespective of the initial oxidation state of the iron salts. We can thus infer a partial oxidation of ferrous ions to ferric ones during the preparation.

4. Conclusions

DR UV-Vis, EPR, HRTEM and IR techniques were employed to describe the nature and distribution of Fe species in clinoptilolite natural zeolites and their modification as a consequence of hydrothermal treatments. Noticeably, the employed spectroscopic and structural techniques gave complementary information. For instance oligomeric Fe_xO_y clusters and Fe_2O_3 nanoparticles could be monitored by UV-Vis spectroscopy, but were too small for HRTEM detection. Moreover, the ferromagnetic character of these clusters (likely ascribable to magnetite-like moieties) allowed EPR investigation. This study showed that a controlled removal and reinsertion of iron is possible by hydrothermal treatments, leading to different results in terms of structure and nuclearity of Fe^{3+} ions and Fe_xO_y/Fe_2O_3 clusters/particles. Moreover, IR gave a clear-cut evidence about the insertion of Fe^{3+} ions in isolated framework positions, resulting in additional Brønsted Si(OH)Fe sites, after hydrothermal treatments with iron salts.

These results allow to get some conclusions on the influence of hydrothermal treatments and on the role of iron precursors. The first treatment in orthophosphoric acid has three main effects: i) removal of the vast majority of iron, ii) partial amorphisation of the zeolite tuff and iii) increase of the zeolite defectivity. This can be easily explained by the very small size of iron oxide nanoparticles, which can be thus dissolved in the mild acid conditions. Moreover, the phenomenon of acid induced dealumination, increasing defectivity is well known for zeolites.

More interesting is the effect of the hydrothermal treatments with iron salts. When ferrous salt is employed, highly dispersed species are observed, mainly in the 3+ oxidation state, while the employ of ferric salt results in higher loading and clustering. This clearly show the oxidation of Fe^{2+} ions to Fe^{3+} in the acid solution. However, the higher dispersion suggests that the oxidation process is gradual and partially prevents agglomeration.

More importantly, the presence of isolated Fe^{3+} ions in the proximity of highly defective framework sites, created by the acid environment, favours a chemical reactivity between the two, resulting in the iron insertion in framework positions. To our knowledge, this is the first evidence

for this kind of mechanism in a preformed zeolite structure, opening new perspectives about the flexibility and reactivity of microporous frameworks. Moreover, this study points to the potentiality of natural zeolites for technological applications, particularly catalysis, where the presence of highly dispersed redox sites within microporous cavities could be exploited for selective oxidation reactions or photocatalytic degradations.

Acknowledgements

F. Chavez-Rivas and R. Zamorano-Ulloa acknowledge the support of COFAA-IPN. This research was partially supported by Project IN110608 of DGAPA-UNAM and Project 102907 of CONACYT, Mexico. F. Chavez-Rivas acknowledge technical support from Ignacio Colin Duran from ESFM-IPN and Dr. Vasudev Shetti of the Department of I.F.M. from the University of Turin, Italy. Prof. Mario Chiesa is gratefully acknowledged for fruitful discussions.

Figure captions

Figure 1. DR UV-Vis spectra of a) NZ (full), b) OPAZ (dashed-dotted), c) Fe2+-OPAZ (dashed) and d) Fe3+-OPAZ (dotted).

Figure 2. Spectral deconvolution of the DR UV-Vis spectrum of Fe2+-OPAZ: Gaussian components and resulting absorption (dashed curve).

Figure 3. EPR spectra of NZ sample measured between 300 and 77 K.

Figure 4. EPR spectra of Fe2+-OPAZ measured between 220 and 110K. Inset reports the low field signals measured between 170 and 130 K.

Figure 5. EPR spectra of hydrated NZ, OPAZ, Fe2+-OPAZ and Fe3+-OPAZ samples measured at 180 K.

Figure 6. HRTEM images of samples a) NZ, b), OPAZ and c-d) Fe2+-OPAZ.

Figure 7. FTIR spectra in the hydroxyl stretching region of a) NZ, b) OPAZ, c) Fe2+-OPAZ and d) Fe3+-OPAZ samples before and after CO dosage at 110 K (full and broken lines, respectively. Inset: difference spectra (CO adsorption minus zeolite before adsorption) of Fe2+-OPAZ and Fe3+-OPAZ. Samples were previously outgassed and oxidized at 550 °C.

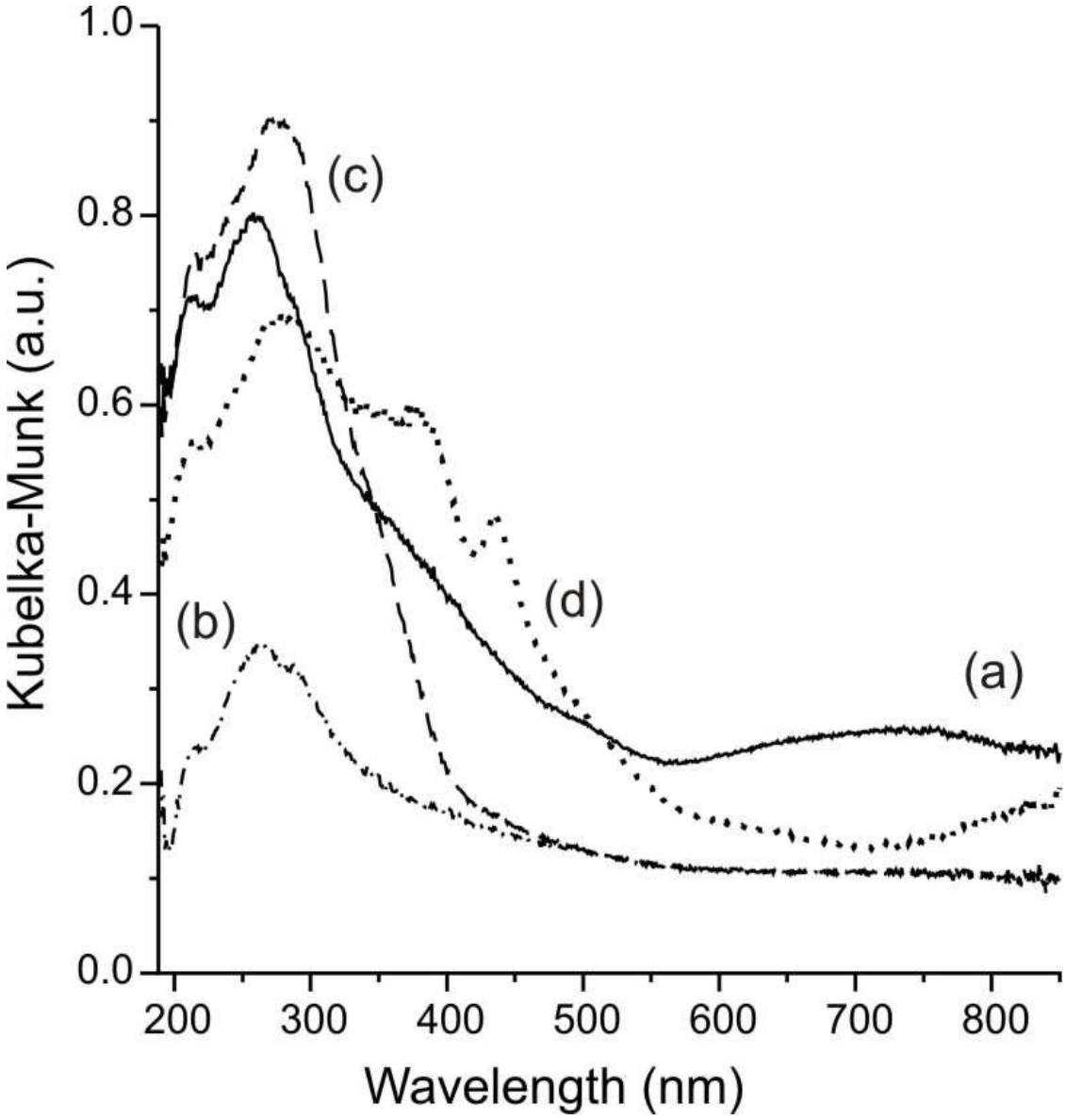
1.0
0.8
0.6
0.4
0.2
0.0
Kubelka-Munk (a.u.)
200
300
400
500
600
700
800
Wavelength (nm)
(a)
(b)
(c)
(d)

Figure 1

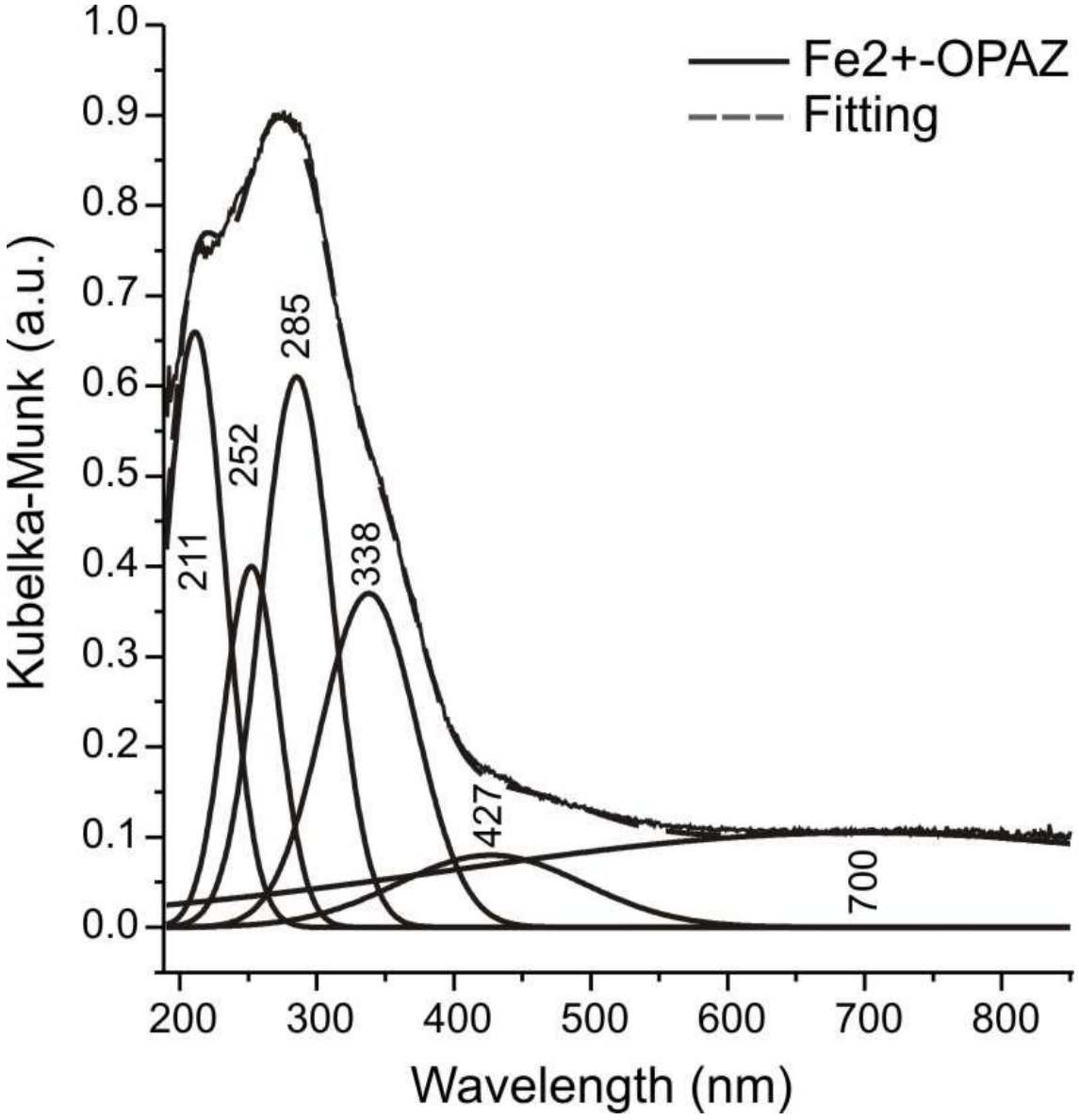
Fe2+-OPAZ
Fitting
Kubelka-Munk (a.u.)
Wavelength (nm)
211
252
285
338
427
700
1.0
0.9
0.8
0.7
0.6
0.5
0.4
0.3
0.2
0.1
0.0
200
300
400
500
600
700
800

Figure 2

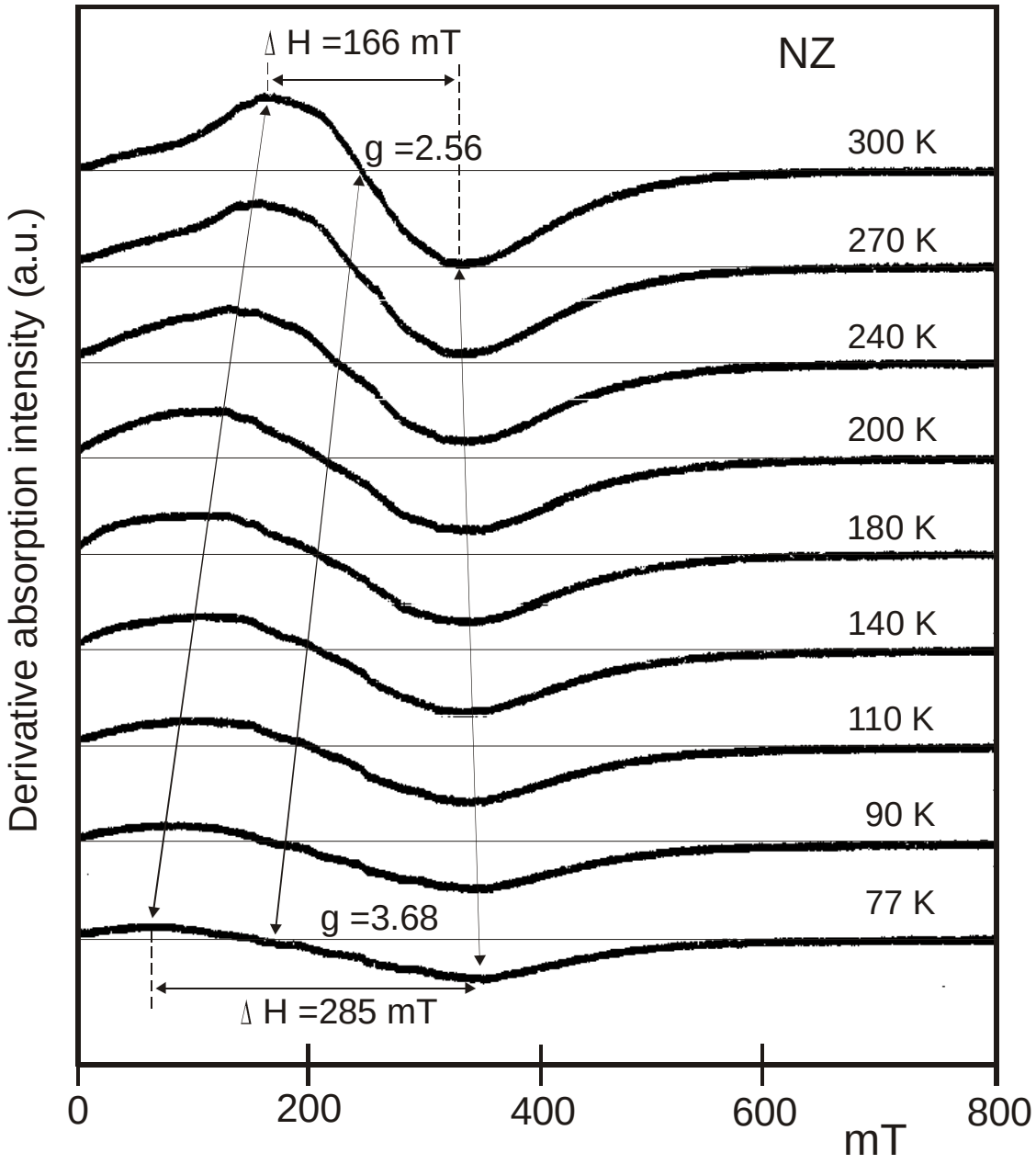
Δ H =166 mT
NZ
g =2.56
300 K
270 K
240 K
200 K
180 K
140 K
110 K
90 K
77 K
g =3.68
Δ H =285 mT
Derivative absorption intensity (a.u.)
0
200
400
600
800
mT

Figure 3

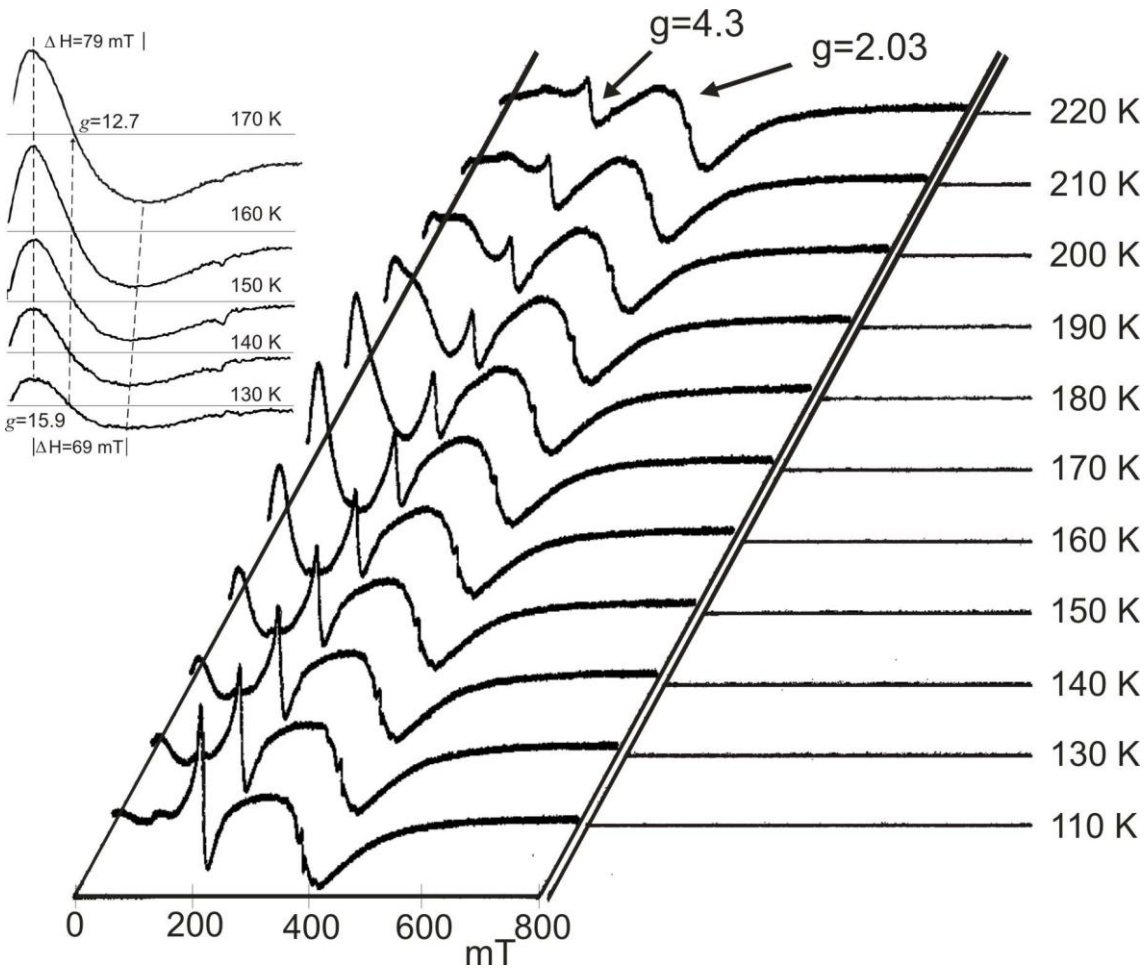
ΔH=79 mT
g=12.7
170 K
160 K
150 K
140 K
130 K
g=15.9
ΔH=69 mT
g=4.3
g=2.03
220 K
210 K
200 K
190 K
180 K
170 K
160 K
150 K
140 K
130 K
110 K
0
200
400
600
800
mT

Figure 4

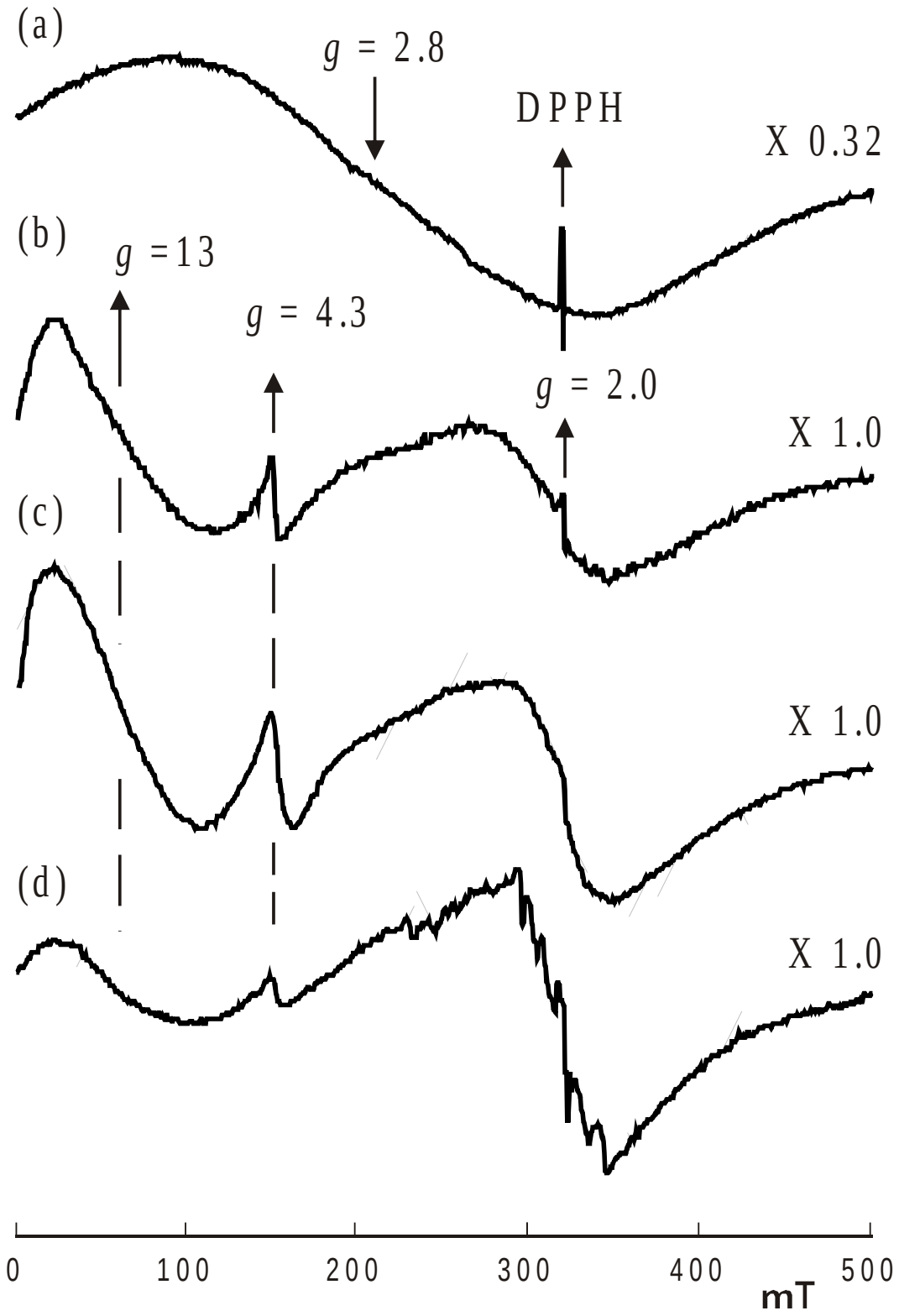
(a)
g = 2.8
DPPH
X 0.32
(b)
g =13
g = 4.3
g = 2.0
X 1.0
(c)
X 1.0
(d)
X 1.0
0
100
200
300
400
500
mT

Figure 5

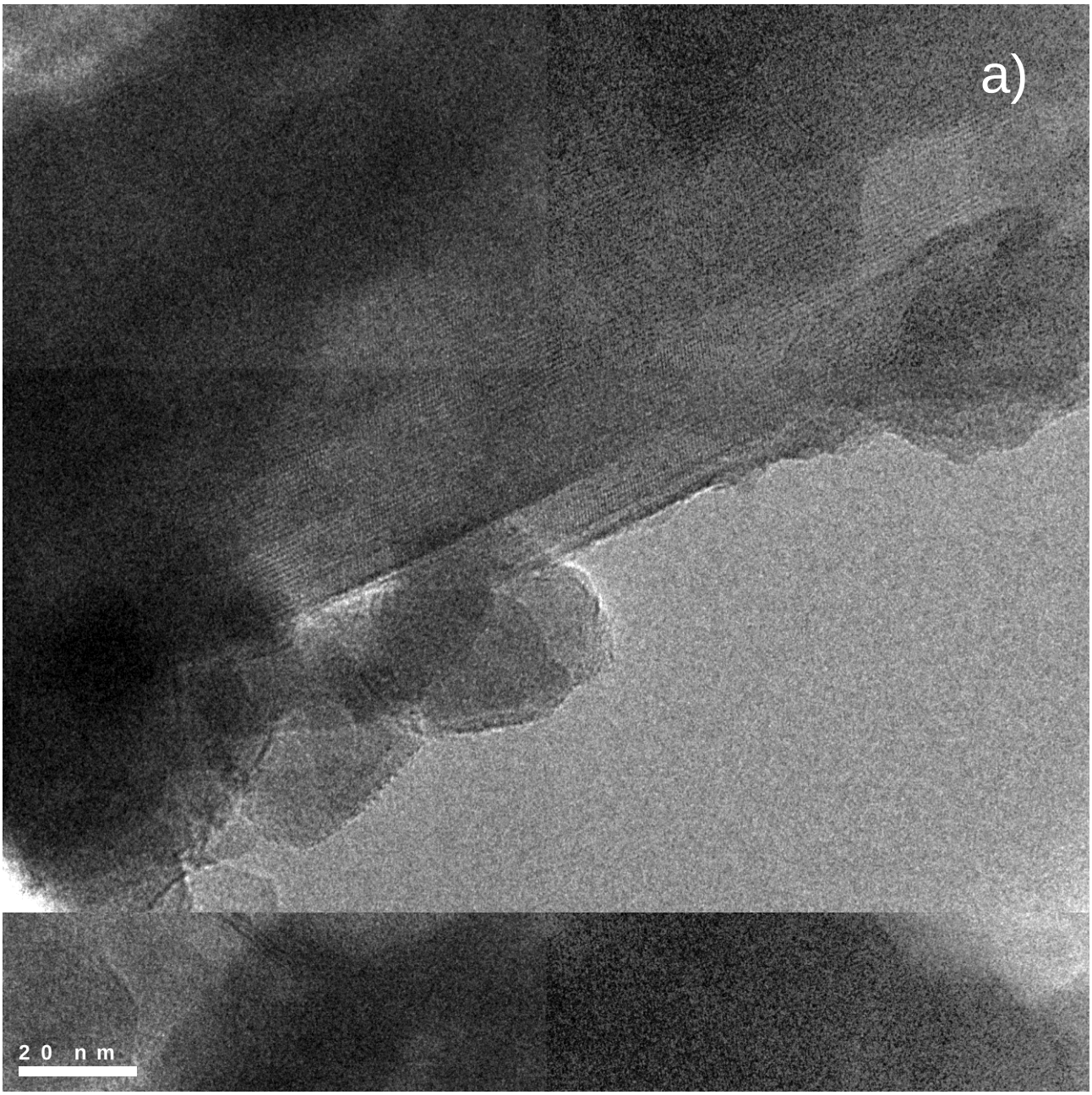
a)
20 nm

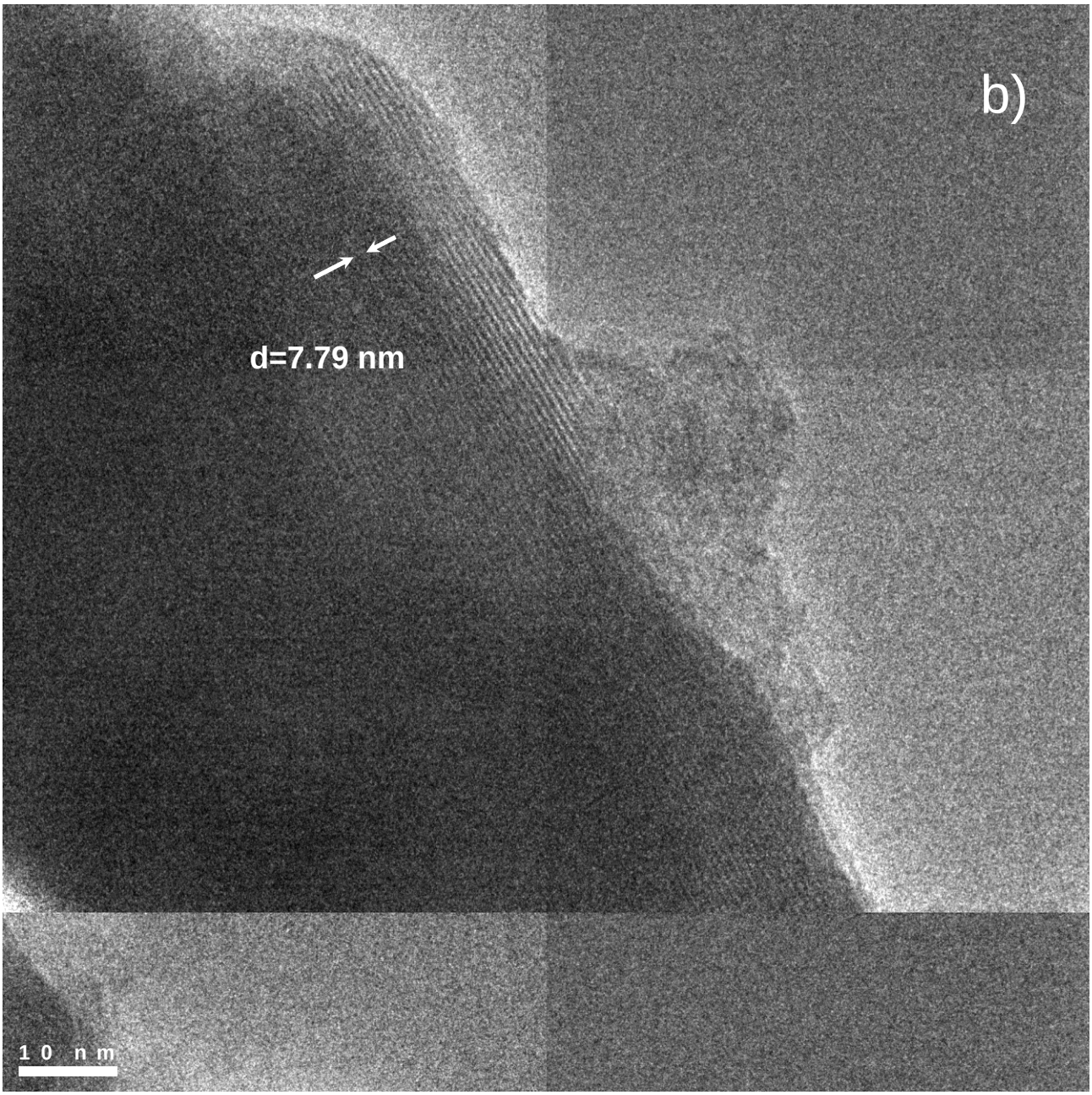
b)
d=7.79 nm
10 nm

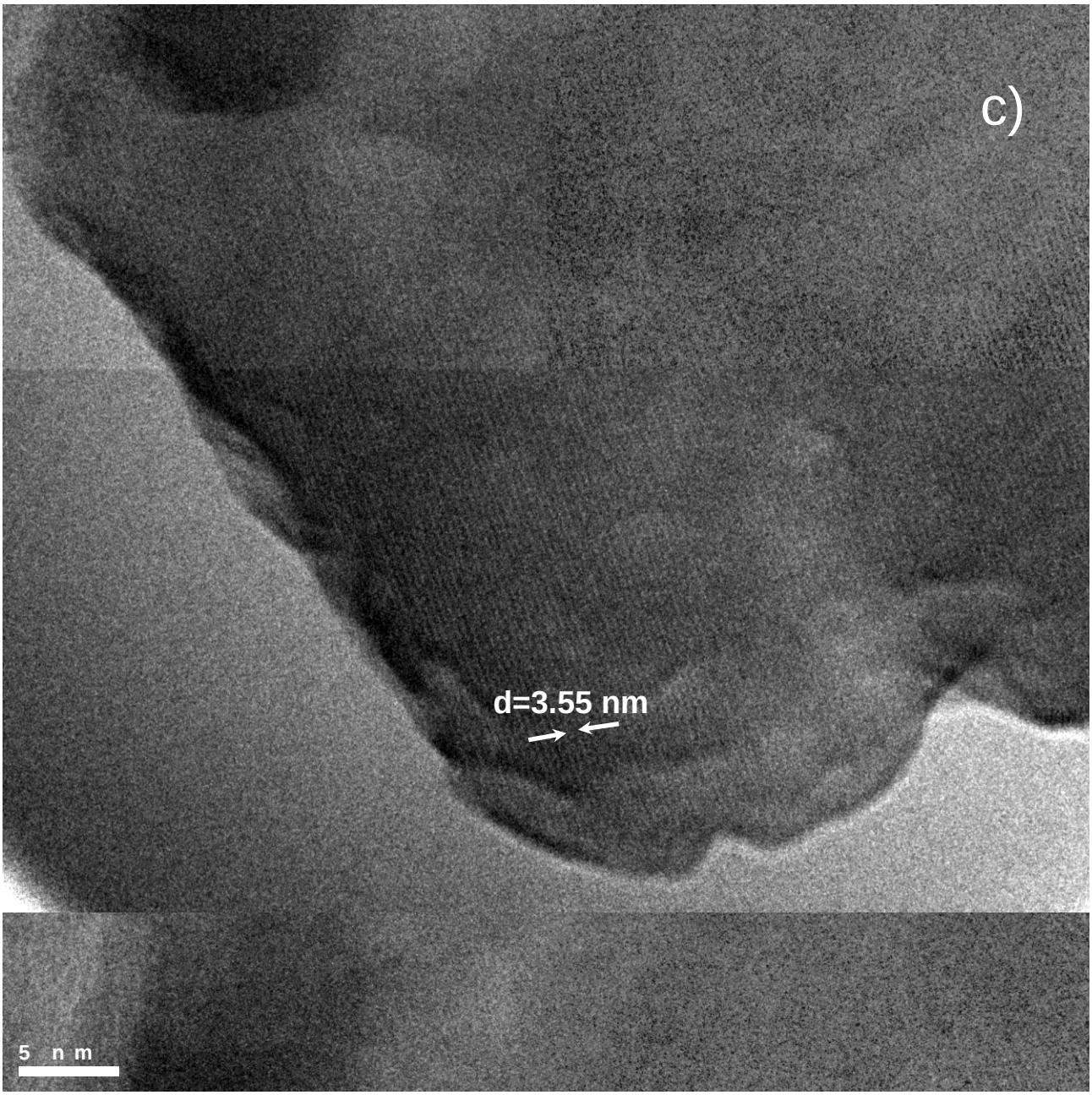
c)
d=3.55 nm
5 n m

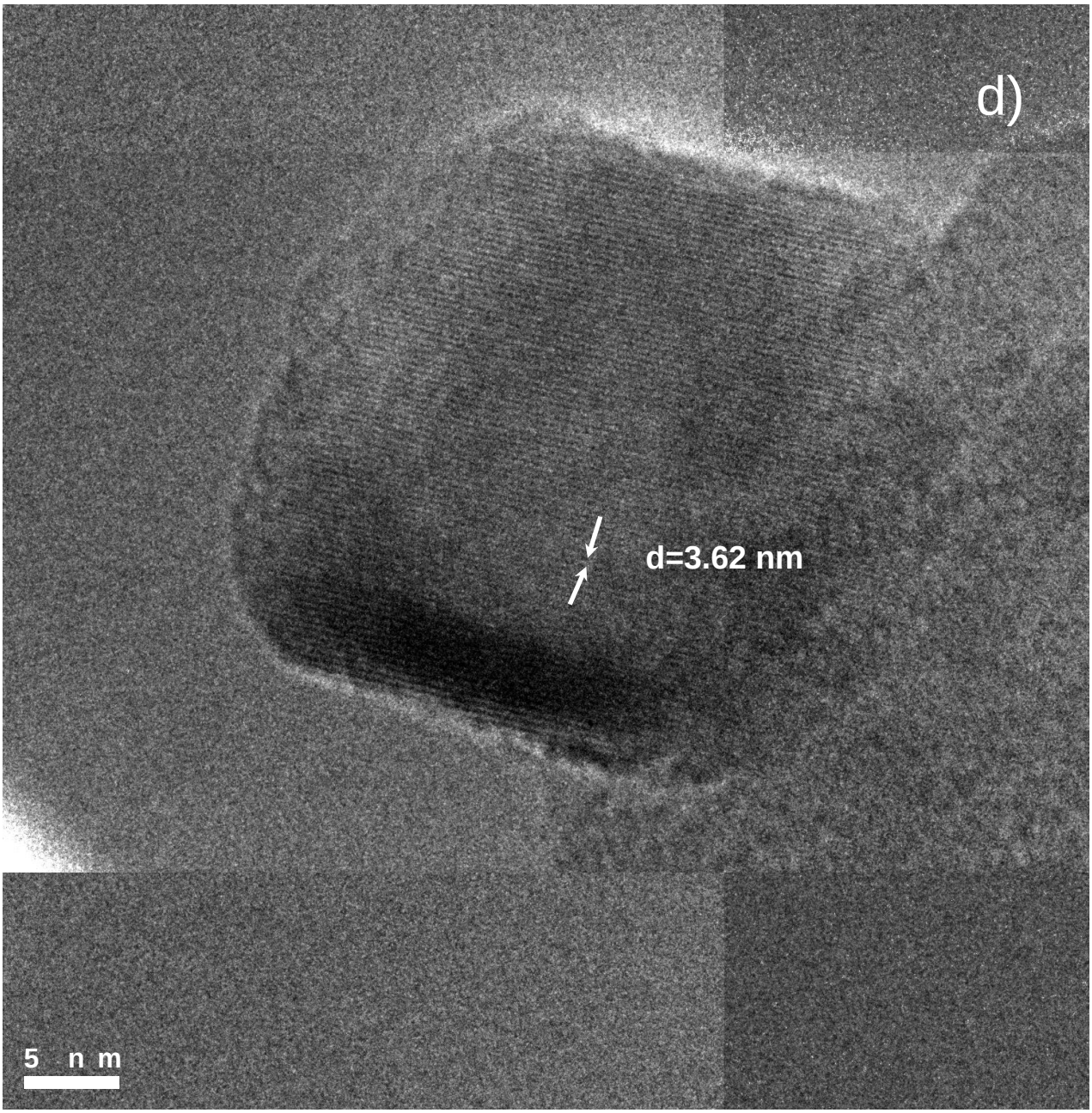

Figure 6

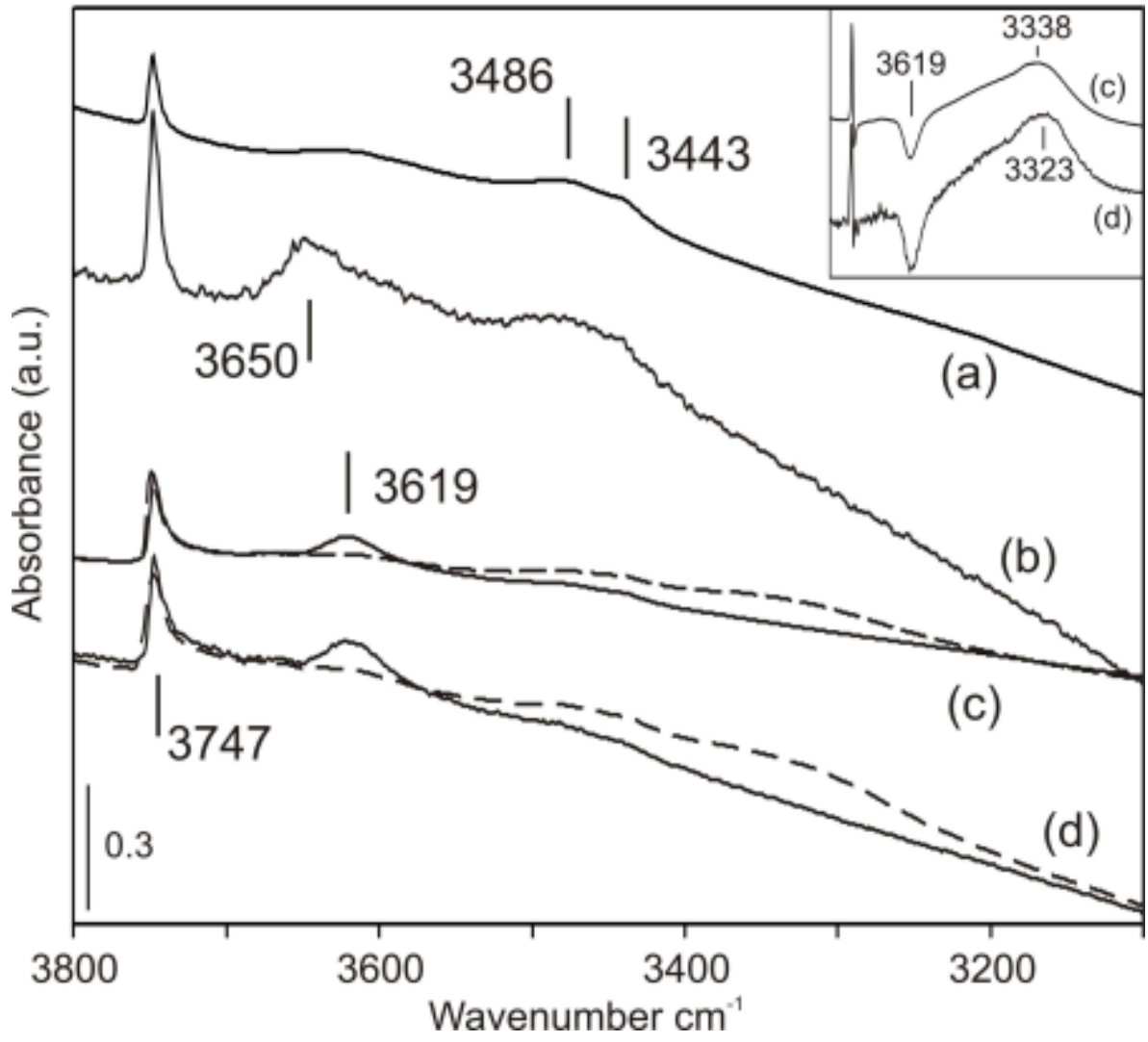
3486
3443
3650
(a)
3619
(b)
3747
(c)
0.3
(d)
3800
3600
3400
3200
Wavenumber cm-1
Absorbance (a.u.)
3338
3619
(c)
3323
(d)

Figure 7

References

[1] C. Colella; Stud. Surf. Scie. Catal. 125 (1999) 641.

[2] D.W. Breck, Zeolite Molecular Sieves. Structure, Chemistry and Use, A Wiley-Interscienc Publication, John Wiley & Sons: New York, 1974.

[3] Atlas of Zeolite Structure Types, 5th revised edition, (Ch. Baerlocher, W.M. Meier and D.H. Olson, Eds.), 2000.

[4] Ph. Moriarty, Rep. Progr. Phys. 64 (2001) 297.

[5] G. A. Ozin, Chem. Commun. (2000) 419.

[6] C. N. R. Rao, J. Mater. Chem. 9 (1999) 1.

[7] G. Vezzalini, FEZA 4th Euroworkshop, Natural Zeolites: Occurrence, Properties, Use, Lectures and Poster Abstracts, 19-21 sept., Ischia (Italia). 1997.

[8] J. M. Thomas, Angew. Chem. Int. Ed. 38 (1999) 3588.

[9] M. Anpo, J. M. Thomas, Chem. Commun. (2006) 3273.

[10] G.I. Panov, G.A. Sheveleva, A.S. Kharitonov, V.N. Romannikov, L.A. Vostrikova, Appl. Catal. A 82 (1992) 31.

[11] L. Kiwi-Minsker, D.A. Bulushev, A. Renken, J. Catal. 219 (2003) 273.

[12] G. Berlier, G. Spoto, S. Bordiga, G. Ricchiardi, P. Fisicaro, A. Zecchina, I. Rossetti, E. Selli, L. Forni, E. Giamello, C. Lamberti, J. Catal. 208 (2002) 64.

[13] G. Grubert, M.J. Hudson, R.W. Joyner, M. Stockenhuber, J. Catal. 196 (2000) 126.

[14] A. Zecchina, M. Rivallan, G. Berlier, C. Lamberti, G. Ricchiardi, Phys. Chem. Chem. Phys. 9 (2007) 3483.

[15] M.-T. Nechita, G. Berlier, G. Ricchiardi, S. Bordiga, A. Zecchina, Catal. Lett. 103 (2005) 33.

[16] G.D. Pirngruber, J.A.Z. Pieterse, J. Catal. 237 (2006) 237.

[17] G. Rodriguez-Fuentes, L.C. de Menorval, E. Reguera, F. Chavez Rivas. Micropor. Mesopor. Mater. 111 (2008) 577.

[18] G. Rodríguez-Fuentes, E. Mora, J.C. Torres, N. Vega, Cuban Patent Application No. 2000-0221.

[19] Manual Jeol, Es-Prit Series, ESR data system (System version 1.6). Simulation, No. ER630001-/631001-1. 1991.

[20] G. Berlier, PhD. thesis in Chemical Science, specialty Physical Chemistry (2001).

[21] S. Bordiga, R. Buzzoni, F. Geobaldo, C. Lamberti, E. Giamello, A. Zecchina, G. Leofanti, G. Petrini, G. Tozzolay, G. Vlaic, J. Catal. 158 (1996) 486.

[22] Y. Li, Z. Feng, H. Xin, F. Fan, J. Zhang, P. C. M. M. Magusin, E. J. M. Hensen, R. A. van Santen, Q. Yang, C. Li, J. Phys. Chem. B 110 (2006) 26114.

[23] L. Căpek, V. Kreibich, J. Děděcek, T. Grygar, B. Witcherlová, Z. DSobalík, J.A. Martnes, R. Brosius, V.Takarova, Microporous Mesoporous Mater. 80 (2005) 279.

[24] M. Santhosh Kumar, M. Schwidder, W. Grünert, A. Brückner, J. Catal. 227 (2004) 384.

[25] J. Long, X. Wang, Z. Ding, Z. Zhang, H. Lin, W. Dai, X. Fu, J. Catal. 264 (2009) 163.

[26] L. Li, Q. Shen, J. Li, Z. Hao, Z. P. Xu, G.Q. Max Lu, Appl. Catal. A 344 (2008) 131.

[27] D.M. Sherman, T.D. Waite, Amer. Mineral. 70 (1985) 1262.

[28] N. Malengreau, J.P. Muller, G. Calas, Clays Clay Miner. 42 (1994) 137.

[29] H. Fischer, J. Luster, A.U. Gehring, Geophys. J. Int. 169 (2007) 909.

[30] A.U. Gehring, H. Fischer, M. Louvel, K. Kunze, P.G. Weidler, Geophys. J. Int. 179 (2009) 1361.

[31] Yu.L. Raikher, V.I. Stepanov, J. Magn. Magn. Mater. 242–245 (2002) 1021.

[32] V.K. Sharma and F. Waldner, J. Appl. Phys. 48 (1977) 4298.

[33] D.M.S. Esquivel, D. Acosta-Avalos, L.J. El-Jaick, A.D.M. Cunha, M.G. Malheiros, E. Wajnberg, Nature 86 (1999) 30.

[34] B.P. Weiss, S.S. Kim, J.L. Kirschvink, R.E. Koppa, M. Sankaran, A. Kobayashi, A. Komeili. Earth Planet. Sci. Lett. 224 (2004) 73.

[35] Yu.A. Koksharov, D.A. Pankratov, S.P. Gubin, I.D. Kosobudsky, M. Beltran, Y. Khodorkovsky, A.M. Tishin J. Appl. Phys. 89 (2001) 2293.

[36] M. Fittipaldi, L. Sorace, A.-L. Barra, C. Sangregorio, R. Sessoli, D. Gatteschi, Phys. Chem. Chem. Phys. 11, (2009) 6555.

[37] A.K. Sinha, C.V.V. Satyanarayana, D. Srinivas, S. Sivasanker, P. Ratnasamy. Microporous Mesoporous Mater. 35–36 (2000) 471.

[38] R. Ganesan, B. Viswanathan. J. Mol. Catal. A 223 (2004) 21.

[39] Database of Zeolite Structures of the International Zeolite Association: http://www.iza-structure.org/databases/

[40] A. Zecchina, S. Bordiga, G. Spoto, L. Marchese, G. Petrid, G. Leofanti, M. Padovan. J. Phys. Chem. 96 (1992) 4991..

[41] S. Tosoni, B. Civalleri, F. Pascale, P. Ugliengo. J. Phys.: Conf. Ser. 117 (2008) 012026.

[42] A. Zecchina, S. Bordiga, G. Spoto, D. Scarano, G. Petrini, G. Leofanti, M. Padovan, C. Otero Areàn, J. Chem. Soc. Faraday Trans. 88 (1992) 2959.

[43] F. Geobaldo, S. Fiorilli, B. Onida, G. Giordano, A. Katovic, E. Garrone, J. Phys. Chem. B 107 (2003) 1258.

[44] C. Otero Areàn, G. Turnes Palomino, F. Geobaldo, A. Zeccchina, J. Phys. Chem. 100 (1996) 6678.

[45] P. Strode1, K.M. Neyman, H. Knözinger, N. Rösch, Chem. Phys. Lett. 240 (1995) 547.

[46] H. Knözinger, S.Huber, J. Chem. Soc., Faraday Trans. 94 (1998) 2047.

[47] G.A.V. Martins, G. Berlier, S. Coluccia, H. O. Pastore, G.B. Superti, G. Gatti, L. Marchese, J. Phys. Chem. C 111 (2007) 330.

Supplementary information

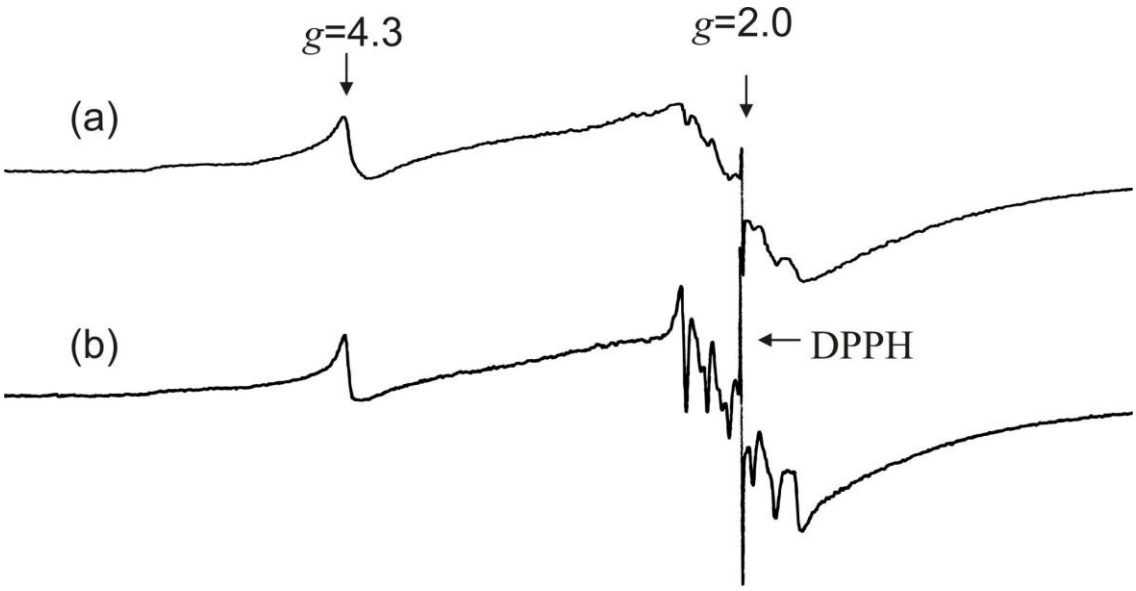

Figure S1. EPR spectra of Fe^{3+}-OPAZ samples measured at 77 K: (a) hydrated and (b) dehydrated at 393 K for 5 h.

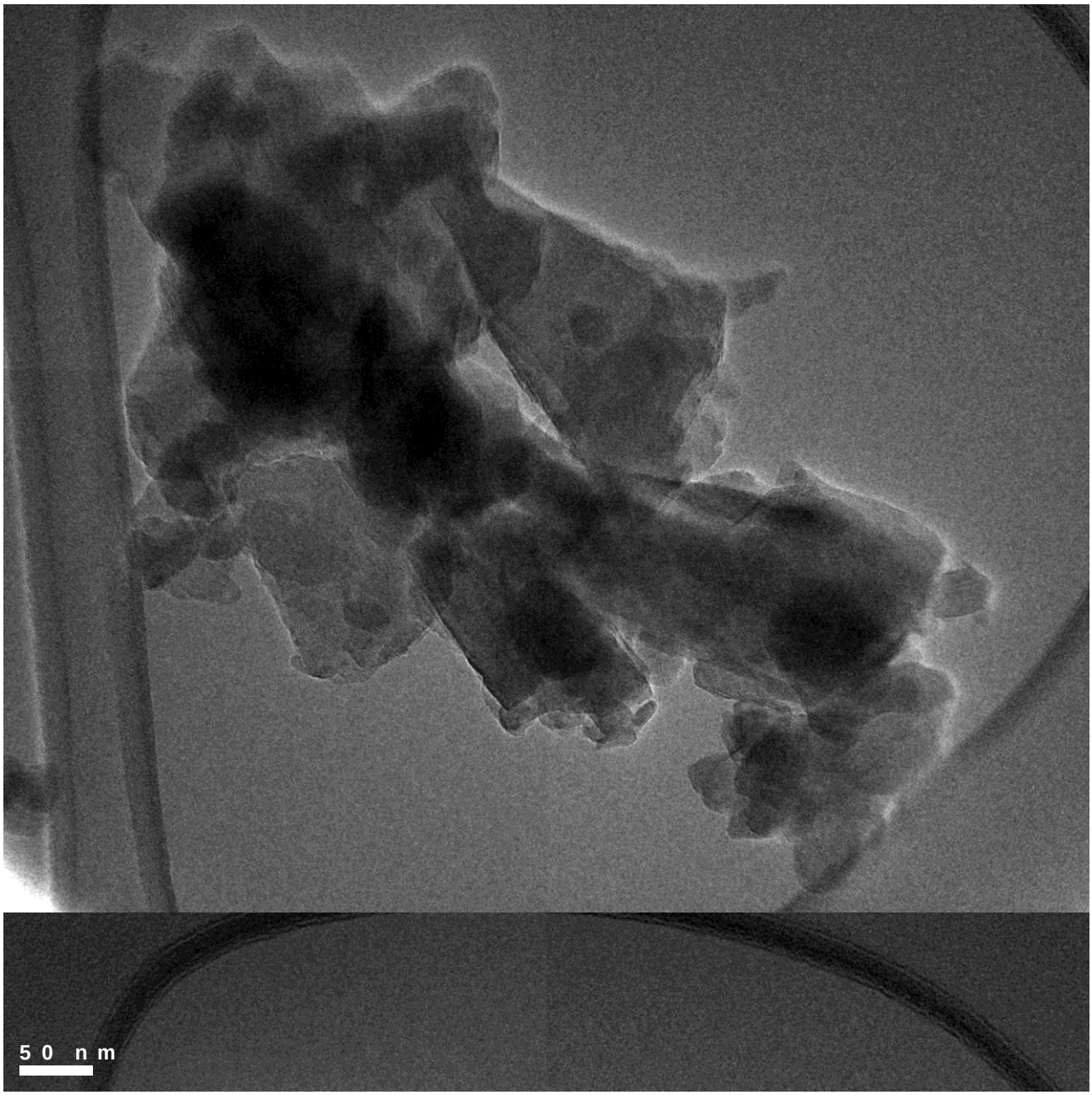

Figure S2. Low magnification TEM image of NZ sample, showing an agglomerate 700 x 300 nm in size.

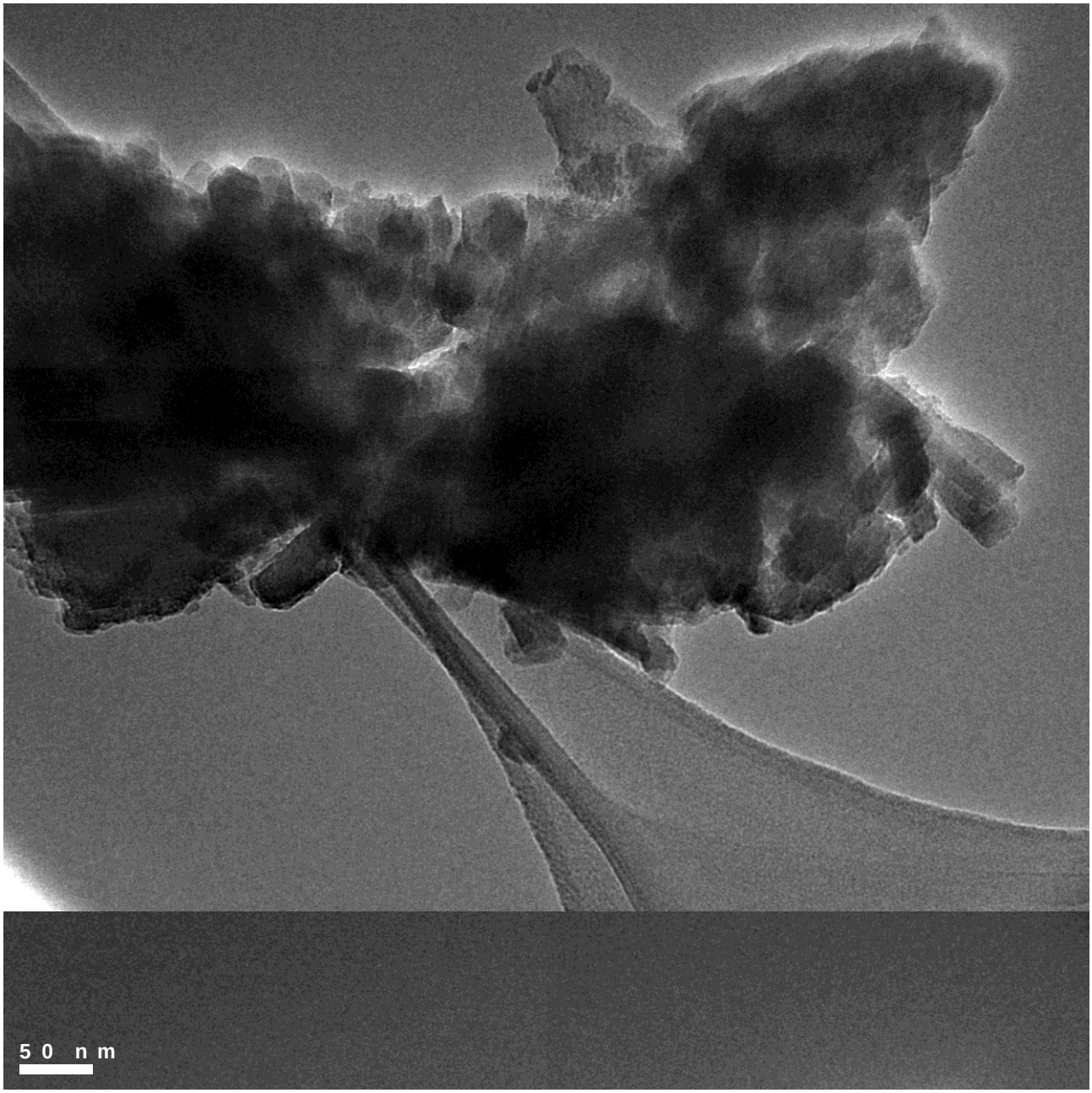

Figure S3. Low magnification TEM image of OPAZ sample, showing an agglomerate 700 x 300 nm in size.

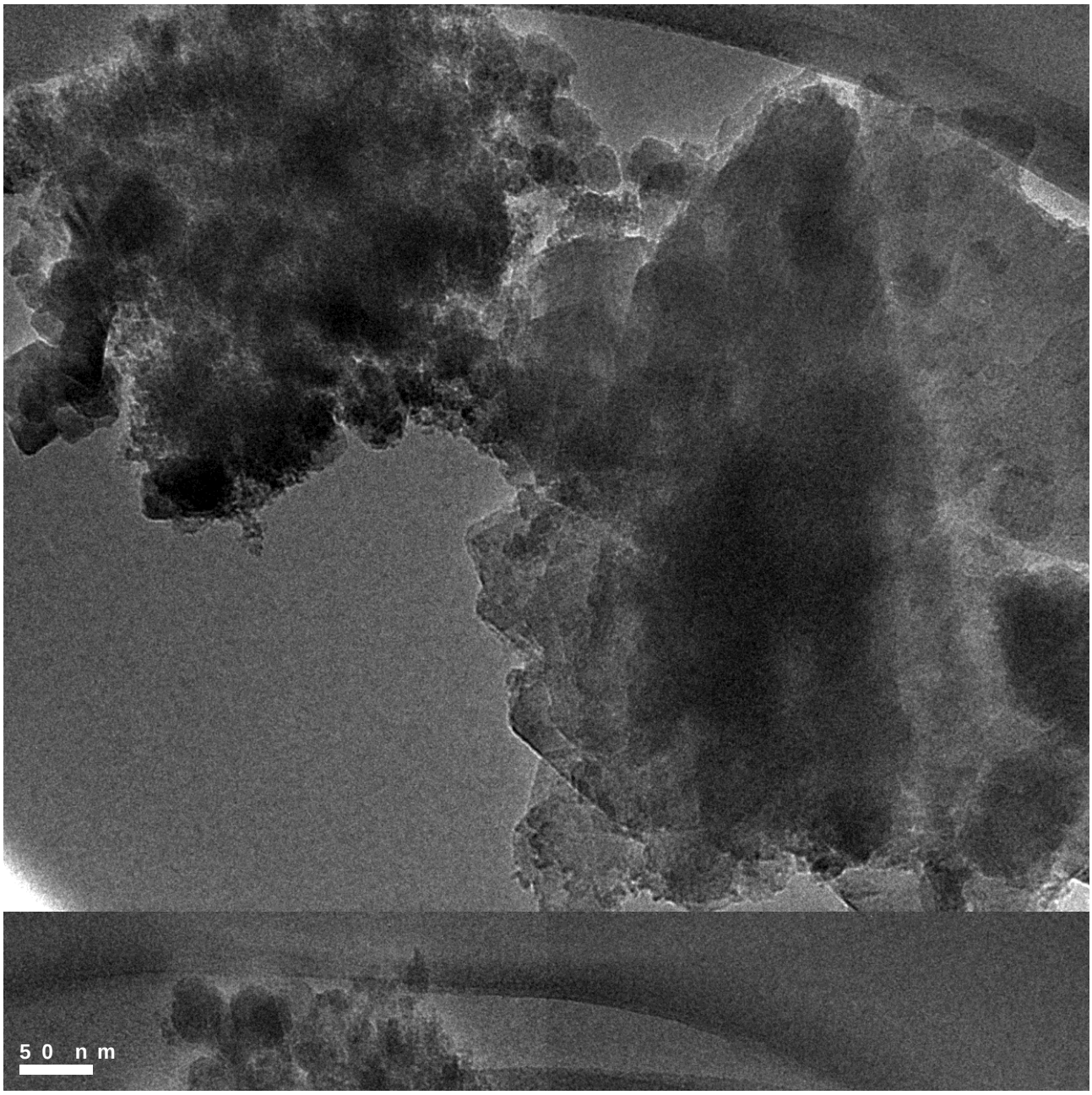

Figure S4. Low magnification TEM image of OPAZ sample, showing large agglomerates covered by an amorphous phase.

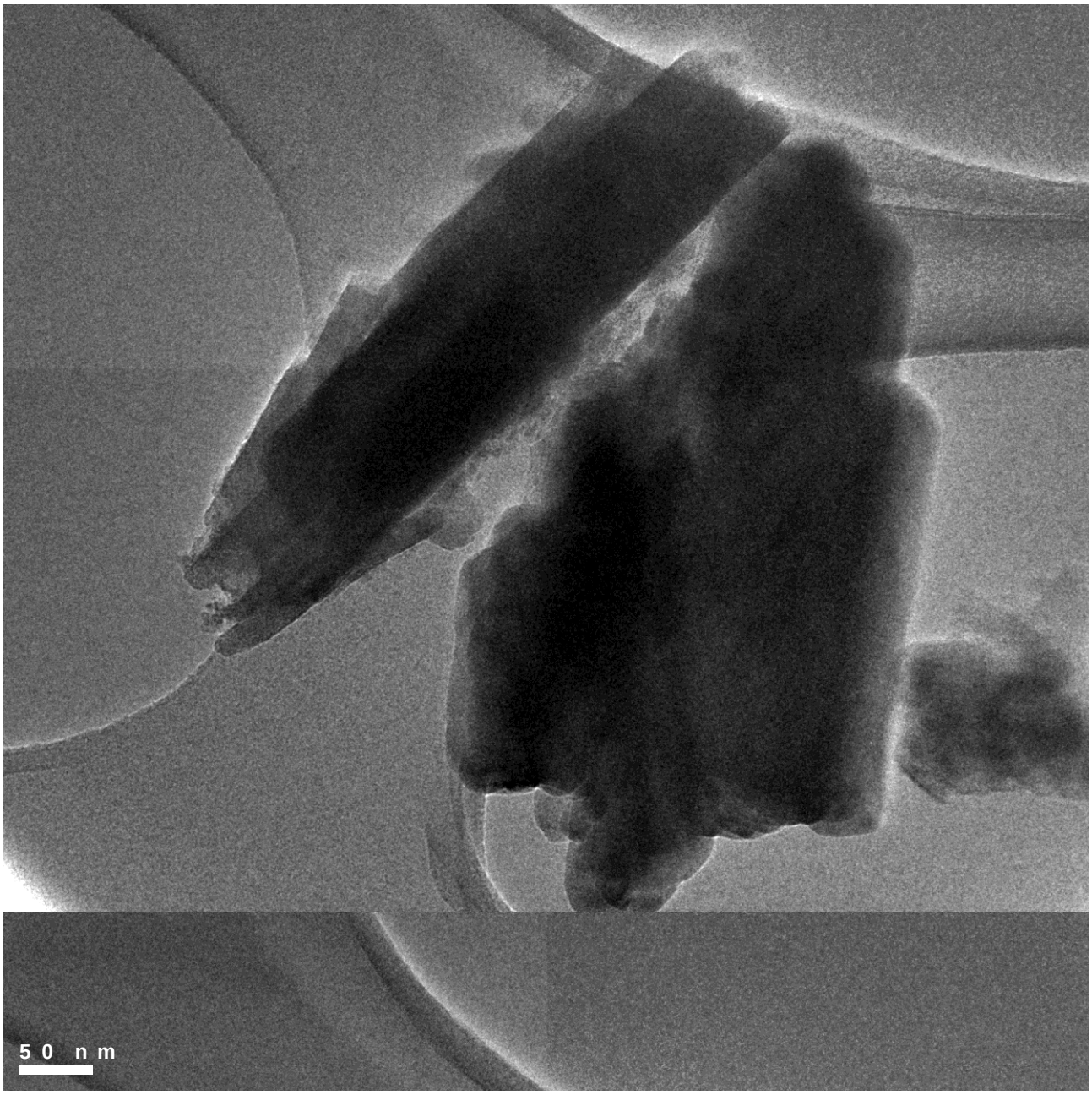

Figure S5. Low magnification TEM image of Fe^{2+}-OPAZ sample, showing elongated agglomerates, with sizes of 500 x 130 and 550 x 300 nm.